Erosion mechanisms of thermally sprayed coatings with multiple phases

Narayanan Ramanujam [1], Toshio Nakamura *

Department of Mechanical Engineering, State University of New York at Stony Brook, Stony Brook, NY 11794, United States

ARTICLE INFO

ABSTRACT

Thermally sprayed coatings are frequently subjected to impacts by small solid particles which induce surface erosion. To identify the physical mechanisms associated with such a material removal process, experimental tests as well as detailed computational analyses of porous coatings containing multiple phases are performed. In the experiments, a gas jet erosion test is conducted to measure material loss of coatings with different mixtures of brittle and ductile phases. The results show higher erosion resistances with small volume fractions of metal phase added to predominantly brittle coatings. Following this outcome, the study is directed toward elucidating the physical mechanisms behind the increased erosion resistance. Here, solid particle impacts are simulated with dynamic finite element analyses where material removals and coating's energy absorption behaviors are closely monitored. Furthermore, parametric study is carried out to quantify effects of cracking resistances and plastic dissipation on the erosion rate. The results reveal synergistic effects of fracture energy and plastic deformation. The combined mechanisms allow greater energy absorptions and enhanced erosion resistance in coatings with mixture of ductile phase. These assessments should offer insights into tailoring coatings with optimized composition of ductile phase to increase their performances. The results are also valuable in understanding foreign object damage (FOD) of coatings.

1. Introduction

Erosion of thermally sprayed ceramic coatings due to solid particles has been a persistent and serious problem in engineering applications that require high temperature resistances. Coatings optimized to provide improved erosion resistance has economic and industrial significance [1,2]. A possible design strategy is to introduce small amounts of metallic phase into mostly brittle ceramic coatings without significantly reducing their high temperature integrity. Since such heterogeneous coatings possess unique and complex microstructures, the physical mechanisms responsible for increased erosion resistances are yet to be clarified. To understand these mechanisms, modeling of material removal and characterization of damage process under dynamic impacts of solid particles is necessary. The results may help to identify the optimal ductile material phase and its mixture in the coatings.

Extensive research has been performed on erosion of homogeneous material systems including experimental and analytical studies although the physical mechanisms involved are not yet completely understood (for example [1,3]). However for inhomogeneous materials, even for those with just pores (e.g., thermally sprayed YSZ coatings), past studies are limited. In general, pores accelerate coating erosion due to crushing of material under impacting solid particles. However, such mechanisms are complex and not yet understood [4,5].

To compensate the reduction of erosion resistance due to porosity, ductile phase addition has been identified as cost-effective option to achieve superior erosion/wear performance [1]. Coatings with multiple or heterogeneous phases are utilized in several applications. For example, carbide based coatings including WC$-$Co and Cr$_3$C$_2$$-$NiCr are used in low and high temperature compressor blades in gas turbine engines, boilers and power plant machinery [2], and also applied in aircraft landing gears [6]. Graphite coatings reinforced with either AlSi or Ni is used for providing a sealing between rotating and stationary parts in aerospace turbine engines [7]. Furthermore, ceramic coatings with NiCrAlY phase are applied as abradable air seals in compressor section of gas turbines [8]. Additions of ductile phase to coatings have also proven to increase the erosion resistances of intermetallic compounds that are used as high temperature gas turbines, corrosion resistant materials, heat treatment fixtures, magnetic materials and hydrogen storage materials [9]. Cermets (ceramic matrix composites) are known to possess higher fracture toughness due to the addition of a second ductile phase. Cook et al. [10] showed doubling of critical stress intensity factor (K_{Ic}) in boride (AlMgB$_{14}$) with addition of Co$-$Mn binder.

Although several researchers have studied the benefits of ductile phase addition on coatings, they are mostly experimental in nature. For wear properties, Yin et al. [11] studied effects of microstructure of Al$_2$O$_3$$-$Al composite coatings deposited by plasma spraying. Dong et al. [12] fabricated Fe$_2$O$_3$$-$Al self reaction composite powders and observed benefits in wear properties due to ductile phase addition. Among others, Chwa et al. [13] studied wear properties of plasma sprayed TiO$_2$$-$Al composite coatings. For solid particle erosion,

Harsha et al. [14] reported the detrimental effects of brittle phase (short glass and carbon fibers) in polyethermide and its composites. Sinmazcelik and Taskiran [15] and undertook similar studies on polyphenylenesulphine composites, and Tsuda et al. [16] investigated sand erosion of glass fiber reinforced epoxy composites. Also, Chen and Li [17] conducted a numerical analysis with complex micro-scale dynamic models to simulate single particle impact related fragmentation on heterogeneous material. However, computational studies on this subject are still limited.

In the present study, solid particle erosion of porous plasma sprayed coatings with heterogeneous microstructure is investigated. First, erosion tests are performed on plasma sprayed YSZ coatings with three different volume fractions of ductile CoNiCrAlY phase. They are subjected to alumina particle impacts and their material removal rates by erosion are measured. Following the experimental tests, finite element models are constructed to simulate the surface erosion by dynamically impacting particles. In addition to monitoring the erosion process, energy transfer from the impacting particle to the coating is closely examined. Although certain features are idealized, the computational analysis is effective in elucidating underlying mechanisms for erosion otherwise not possible from the experimental results. Here, the elastic–plastic properties are assumed for the ductile phase and the material removal process is defined by an imposed fracture criterion. These models explicitly take into account the heterogeneity of coatings based on their actual SEM images. In the computational analysis, single particle impact and multi-particle impacts are simulated. The current study is also helpful in understanding foreign object damage (FOD) of thermally sprayed coatings for turbine blades.
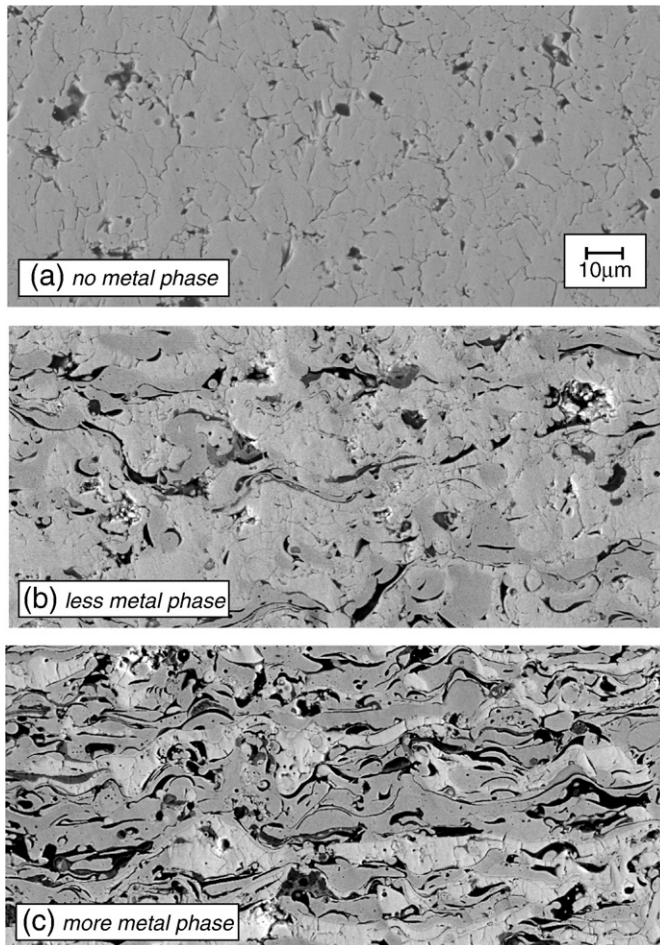

Fig. 1. SEM micrographs of three TS coatings with different compositions.

2. Erosion experiments

2.1. Specimen preparation

Thermal sprayed (TS) coatings are prepared by plasma spraying molten or semi-molten particles of yttria stabilized zirconia (YSZ). For the ones with the ductile phase, CoNiCrAlY powder (Praxair #CO-211) is pre-mixed with fused and crushed YSZ powder (Saint Gobain #HW1532) and sprayed onto steel substrate. For spraying, the PT-F4 gun manufactured by Sulzer Metco Inc. is used. The YSZ powder has the size distribution of 10–75 μm. For CoNiCrAlY feedstock powder, the particle sizes are 5–45 μm. The spraying distance was set at 100 mm with a powder feed rate of 0.5 g/s. Following deposition of thermal sprayed (TS) coatings, specimens are machined to dimensions of 12.5 mm × 25.0 mm. A nominal thickness of coating was 0.7 mm while the steel substrate was 1.3 mm thick. Three different specimens are prepared: one with 100% YSZ without ductile phase, and the others with 20 and 40 wt.% of CoNiCrAlY powder pre-mixed with YSZ powder, respectively.

Scanning electron micrographs (SEM) of cross-section (thickness dimension) of these specimens are shown in Fig. 1. Here they are Specimen A with only YSZ phase (no metal), Specimen B with 20% pre-mix of CoNiCrAlY and Specimen C with 40% pre-mix of CoNiCrAlY phase. Different shades of gray correspond to various material phases. In Specimens B and C, some aluminum (in CoNiCrAlY powder) is oxidized into alumina (Al_2O_3) during the high temperature deposition. In order to clearly see the phases, the SEM micrographs were processed by image analysis and the different phases are highlighted as shown in Fig. 2. In Specimen A (with only YSZ phase), only pores/cracks (white) can be seen in addition to YSZ phase (blue). For the specimens with metal phases (B and C), four separate phases/regions can be observed. They are the YSZ, pores, CoNiCrAlY (red) and oxide (green) phases. Volume fraction of each phase is also computed and shown in Table 1. Note that the volume fractions of CoNiCrAlY do not match with those of pre-deposition powder mixture since some of Al is oxidized to become Al_2O_3. Also, initial mixture is set in weight percent and not in volume percent. Interestingly, the volume fractions of Al_2O_3 phase are about half of those of CoNiCrAlY in the two mixed specimens. Although not shown here, the identity of these phases was confirmed by chemical characterization through energy dispersive spectrometer (EDS).

2.2. Erosion test procedure

Jet nozzle type equipment is set up to conduct erosion test following ASTM standards [18] as shown in Fig. 3(a). Here the erosive particles are chosen as alumina whose sizes are in the range of 20–80 μm with irregular polygonal shapes as shown by the optical image in Fig. 3(b). The inner diameter of nozzle is 1.5 mm while the nozzle length is 37.5 mm. The working distance between nozzle and specimen surface is 10 mm. The air pressure is set at 138 kPa with the mass flow rate of alumina at 21 mg/s. This slightly lower rate (than the standard flow rates) was chosen since TS YSZ coatings erode very quickly compared to other common solid materials (e.g., steel). The lower rate chosen is conservative as any possible particle interaction effects are reduced. The particle velocity measured by particle image velocimetry (by Vision System Inc.) is ~100 m/s. All of the specimens were subjected to the same particle flow rate and velocity. To ensure the accuracy of the present set up, it was tested with a type 316 stainless steel specimen. The resulting mass loss behavior of steel was consistent with the well-documented results [18] under the given particle flow rate and velocity. Subsequently, various TS coating specimens described earlier were tested under the same solid particle impact condition.

2.3. Measured erosion via mass loss

In the present tests, the angle of impact is always set perpendicular to the surface (at 90°). Impacts of alumina particles generate a crater
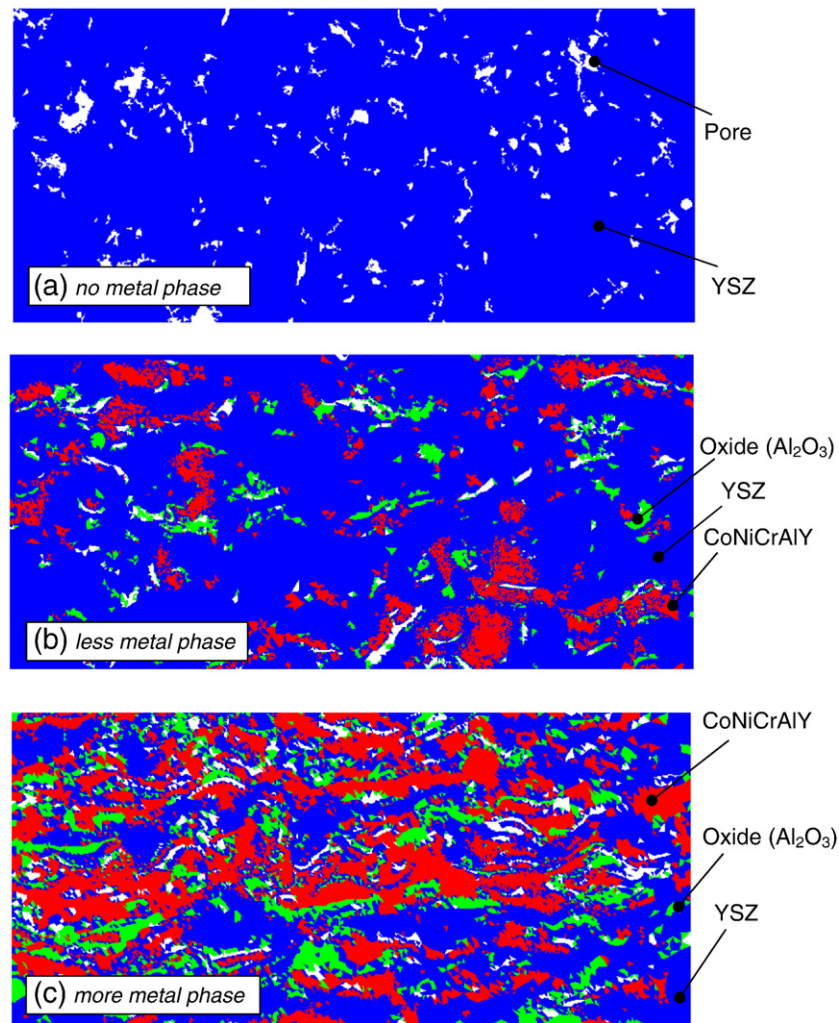
Fig. 2. Various phases within TS coatings are highlighted via image analysis. (For interpretation of the references to color in this figure legend, the reader is referred to the text.)

on the surface of TS specimens as shown in Fig. 4 for Specimen A. Here, a crater radius of about 1 mm and depth of about 140 μm is formed after 40 s exposure to alumina particle impacts. The material removal occurs through cracking and chipping away of YSZ by striking alumina particles. Based on the mass flow rate of 21 mg/s and assumed average particle radius of 25 μm, roughly 80,000 particle strikes occur in a second. This translates to a particle strike at every $t \sim 12.5$ μs. Since the erosion process of a single particle only lasts for a fraction of μs (see Section 4.1) and particles strike over 1 mm radius region, interaction effects among particles can be assumed to be negligible.

The erosion rate is determined by measuring mass change before and after the test. For each specimen, the erosion test is carried out at three different (sufficiently separated) locations. At each location, the test is interrupted and the specimen is removed from the rig every 10 s to measure the current mass. Special care is taken to re-attach the specimen to the previous place so the alumina particles impact at the

same location. The average mass losses for three specimens are shown in Fig. 5(a). Here each error bar is generated from the standard deviation of the three data measurements. Among three tests carried out for each specimen, very small variations are observed for specimens with metal phases (B and C) while the mass loss varies about ±8% for YSZ-only Specimen A. More importantly, the results indicate that the erosion rate is significantly less for TS coatings with the addition of ductile phase (CoNiCrAlY). For Specimen B (with 11% volume fraction of CoNiCrAlY), the mass loss is 55% of that for YSZ-only specimen while it is only 30% of YSZ-only specimen for Specimen C (with 29% of metal phase).

The rates of erosion change somewhat during the test as shown in Fig. 5(b). In general, the rates tend to drop as the specimens are more eroded. This is likely to be caused by changing profile of target surface from planar to concave. Larger initial erosion rates may also be attributed to outcropping of protrusions on the coating surface [1]. This may explain the higher initial erosion rates in all three specimens.

3. Computational approach

In predominantly brittle coatings, it is expected that the material removal occurs through fragmentations or cracking of the ceramic phase. Even in the coatings with ductile phase (i.e., Specimens B and C), cracking through the metal phases is unlikely since their fracture toughness is much greater. Thus, the ductile phases may act as barriers to
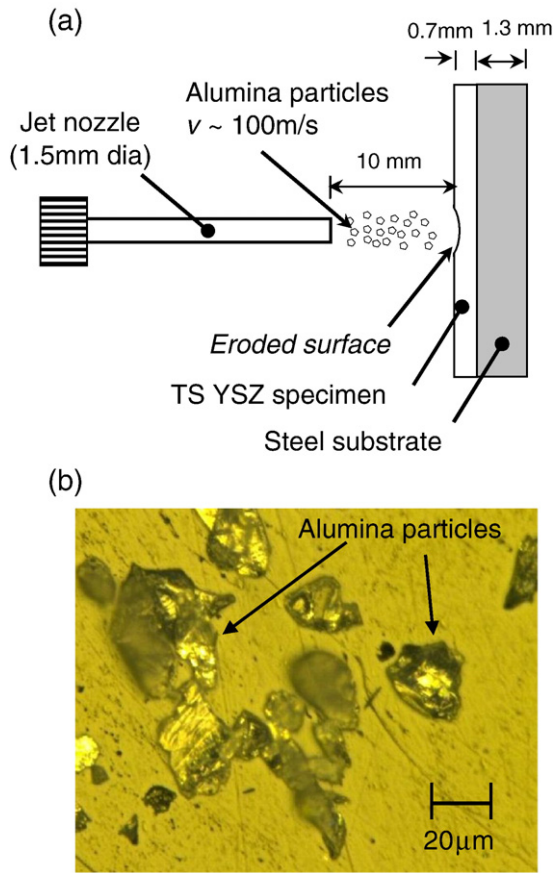
Table 1
Compositions of three TS coating specimens determined by image analysis on SEM micrographs.

Specimens	YSZ	CoNiCrAlY	Al_2O_3	Porosity
A (YSZ-only)	94 ± 1%	0	0	6 ± 2%
B (YSZ/CoNiCrAlY)	81 ± 2%	11 ± 1%	5 ± 1%	3 ± 1%
C (YSZ/CoNiCrAlY)	52 ± 2%	29 ± 1%	14 ± 2%	5 ± 1%

Fig. 3. (a) Schematic of jet nozzle set up for particle impact erosion tests on coatings. (b) Optical image of alumina particles.

crack propagations and also absorb energy through plastic deformation. In order to elucidate such physical mechanisms in the erosion of TS coatings, detailed finite element models are constructed. Since constructing 3D models is not feasible due to computational requirements
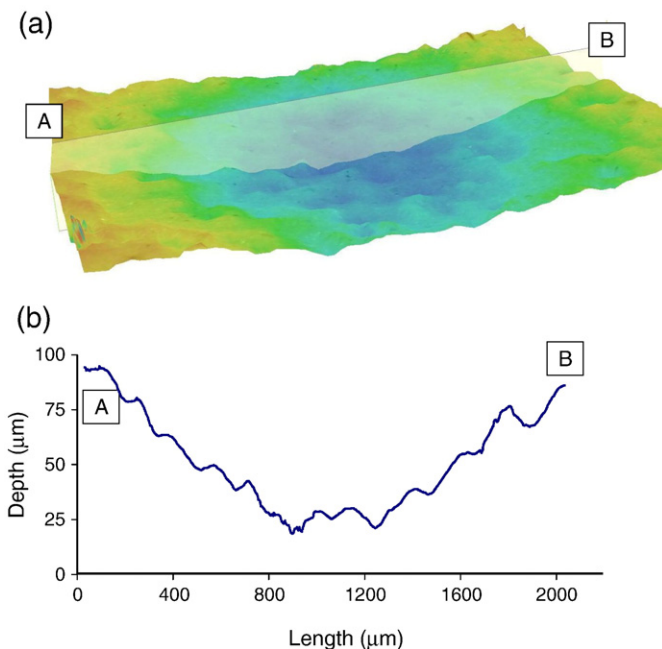

Fig. 4. Surface of eroded coating: (a) 3D image showing a crater. (b) Depth profile showing variations between points A and B.
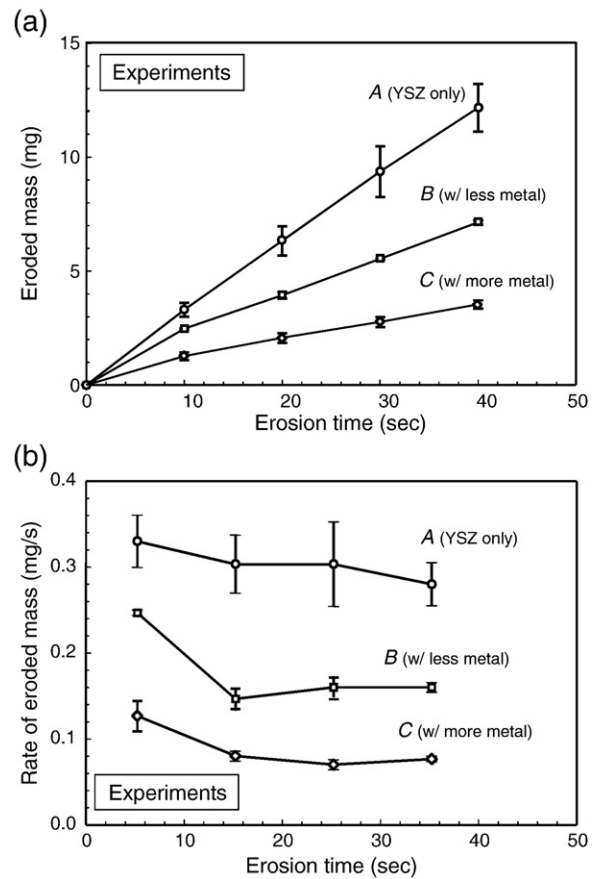

Fig. 5. Measured erosion of different coatings (in terms of mass loss) shown as function erosion times. Particle flow rate is ~21 mg/s with average velocity ~100 m/s. (a) Total mass loss. (b) Rate of mass loss.

and availability of only cross-sectional images (Fig. 1), plane strain models are utilized in the current study. However, some adjustments are made to account for the 3D effects in real erosion as described later. The material removal is simulated through fragmentation of TS coatings via imposed fracture criterion along element boundaries.

3.1. Models with multiple phases

The purposes of computational analysis are to study erosive damage and obtain information that is not apparent from experimental observations. Thus, several parameters are monitored to quantify the effects of metal mixtures, particle speed and other factors. Since the erosion is highly dependent on the heterogeneous nature of microstructures, finite element models are directly generated from SEM micrographs shown in Fig. 1. These images are converted into a finite element mesh by Object-Oriented Finite Element program (OOF) developed at the National Institute of Standards and Technology (NIST). Meshes are generated by progressively refining elements near material interfaces and pores as shown in the inset of Fig. 6 for Specimen *B*. The dimensions of this discretized region are 85 μm × 185 μm. Within this region, the properties of each material phase are assigned separately with corresponding values shown in Table 2. These values are approximated from available data. For an example, the moduli of YSZ and CoNiCrAlY are set lower than those of bulk/fully dense materials since they are deposited by plasma spray and contain very small pores and interfaces that are not modeled in the mesh. However, since larger pores are accounted in the model, these values are set higher than typical effective moduli of TS coatings [19]. The metal phase, CoNiCrAlY, is also modeled as elastic–plastic with bilinear hardening. Note that through
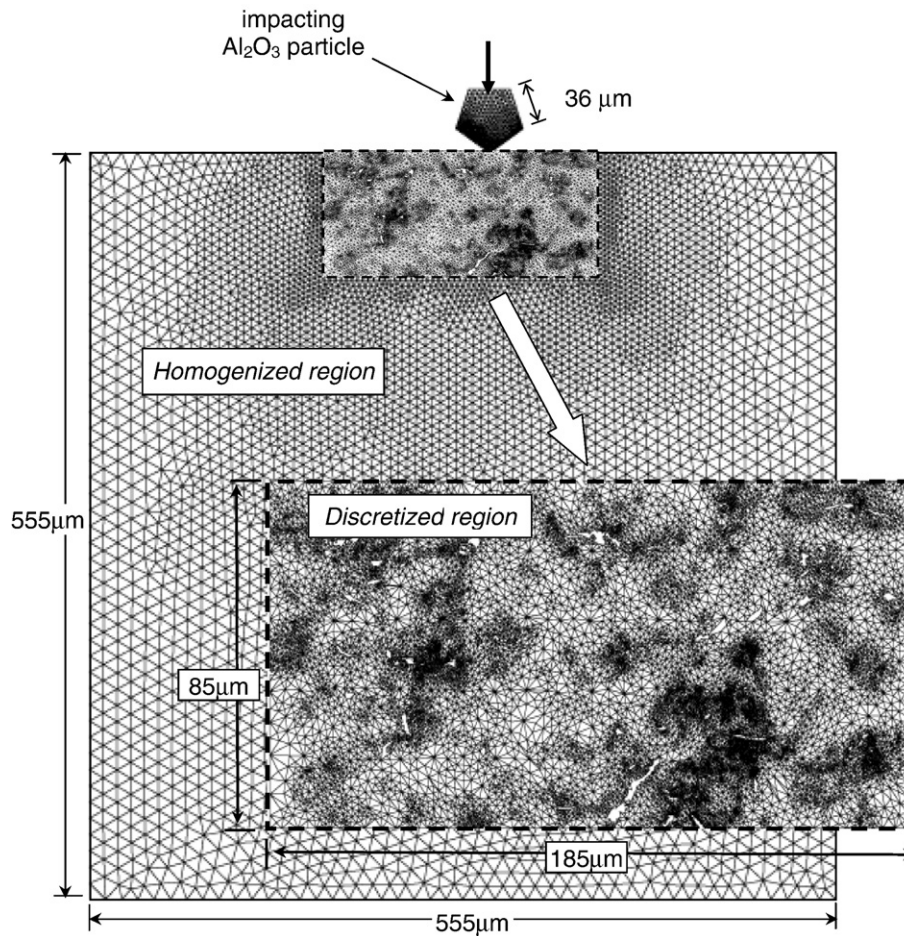
Fig. 6. Finite element mesh for erosion simulation of Specimen *B*. Particle (size ~50 μm) with initial velocity *v* impacts coating surface. Near particle impact region is modeled as heterogeneous media with discrete phases while homogenized model with effective properties is used further away.

separate computations, we have confirmed that small variations in these properties do not affect the material removal rates significantly.

In actual erosion, stress waves generated by a particle impact traverse outward. In general, these waves are not expected to reflect back to the impact region during the impact interval (~0.2 μs). However, because of limited size of FE model, the elastic stress wave reflections from outer boundaries may influence the erosion process during the time interval of interest. In order to minimize such effects, the model is expanded. However expanding the mesh with distinct phases is not practical due to high computational requirements. Instead, a homogenized phase is padded around the discretized region as shown in Fig. 6. Here, the properties of homogenized region are determined as follows. In separate calculations, the discretized model is loaded under tension and its effective stress–strain relation is estimated from the load-displacement results. Since some anisotropy exists along the vertical and horizontal directions, the average result is used to approximate the Young's modulus, yield stress and post-yield

linear hardening modulus as shown in Table 2. For Specimen *A*, only the effective Young's modulus is determined. The mass density is simply determined from the weighted average of all phases including the pores.

Simulations of cracking to cause material removal are modeled by embedded cohesive elements along element boundaries in the discretized region as described in the next section. Separate meshes were constructed for the three specimens. Each mesh contains about 60,000 three-noded triangular elements including 20,000 cohesive elements. Although actual impacting particles in the experiment were variously shaped and sized, they are idealized as pentagons in the simulations (as done by others, e.g., [17]). The regular pentagons (with 72° corner angle) is shown in Fig. 6 with its side length set as 36 μm. This gives a nominal size of 50 μm that represents the mean size of actual alumina particles used in the test. To reduce convergence problems with sharp edges upon contact, the corners of pentagon are slightly blunted with a fillet radius of 0.25 μm.

Contact conditions are enforced between the perimeter of particle and the surface of coating so that particle impact can be simulated. In addition, the contact conditions are imposed between the particle and surfaces of interior elements which are within 55 μm (depth) from the coating surface. The latter contact conditions are necessary to prevent overlapping of the impacting particle with the interior elements as it penetrates through the coating. The properties of alumina particle are shown in Table 2. Here the mass density is intentionally increased by a factor of three to account for the two-dimensional idealization. Unlike the actual tests where the particle impacts at a point (or small area) of coating surface, 2D model assumes the impact to occur over a line (along the out-of-plane direction). This reduces impact stresses and

Table 2
Mechanical properties of various materials.

Phases	E (GPa)	ν	σ_o (MPa)	H (GPa)	ρ (kg/m³)
YSZ	140	0.25	–	–	6000
CoNiCrAlY	120	0.25	230	50	7300
Oxide (Al_2O_3)	250	0.22	–	–	3960
Homogenized *A*	123	0.25	–	–	5270
Homogenized *B*	136	0.24	238	123	5896
Homogenized *C*	129	0.25	238	90.1	5845
Solid Particle (Al_2O_3)	375	0.22	–	–	11,700[a]

[a] Intentionally adjusted to account for 3D effects.

depth in the 2D model as compared to 3D model. To adjust the discrepancy, a larger density is prescribed for the alumina particle. The factor of three is approximated by comparing separately carried out analyses of dynamic impact onto elastic material (without material removal) using axisymmetric and plane strain models. To achieve the same maximum indented displacement as that of the axisymmetric model (a true 3D geometry), the density of particle in plane strain model is increased by three times.

Due to the complexity of actual microstructures, the current computational procedure idealizes certain physical features and makes assumptions on some parameters. Table 3 outlines such assumptions used in the computational models. Here key features such as the heterogeneous and porous microstructures, elastic–plastic behavior of metal phase, and fracturing are accounted to establish suitable material models. Because of these idealizations, it is important to note that the computational results may be compared to the experimental data only qualitatively. However, additional analyses are carried out to confirm that these idealizations do not lead to overly erroneous results.

3.2. Cohesive element formulation for fragmentation

Several computational approaches are possible to simulate material removal process. The choice depends upon the nature of actual material removal. In the present specimens, the cracking of brittle TS zirconia is expected to be the dominant removal mechanism. Thus the fracture criterion based on the surface separation energy is adopted. A different criterion is the one based on critical plastic strain but very large plastic deformation in the metallic phase is not expected to occur prior to fragmentation here. The fracture criterion is implemented in specially formulated 4-noded elements in ABAQUS (with user material). Here the stress–strain relation of these special/cohesive elements follows a prescribed fracture traction–separation law. In many other analyses, 2-noded springs are utilized to simulate such phenomenon but for the dynamic analysis with an explicit time-integration scheme, 4-noded elements are more effective since it requires a diagonalized mass matrix and massless spring elements are not suitable [22].

As noted in [20], the choice of traction–separation relation is not critical. Although several forms of traction–separation relations exist, here the one proposed by Xu and Needleman [21] is chosen. This relation was used effectively for the crack propagation of porous media [22]. This relation utilizes a potential function Φ to represent the energy release during surface separation as,

$$\Phi(\delta_n, \delta_t) = \Gamma_o \left\{ 1 - e^{-\delta_n/\delta_n^*} \left(1 + \frac{\delta_n}{\delta_n^*} \right) e^{-(\delta_t/\delta_t^*)^2} \right\}. \tag{1}$$

Here, δ_n and δ_t are the normal and tangential displacements to fracture surfaces, and δ_n^* and δ_t^* are the reference displacements, respectively. The separation energy per unit area is denoted by Γ_o and

Table 3
Idealization in computational models.

Actual process	Idealization
Solid particle erosion is a 3D phenomenon.	Simulations are carried out with 2D plane strain models.
Point contact occurs between particle and coating.	Line contact is between particle and coating (density of alumina is adjusted).
Fracture parameters of different interfaces are estimated from complex experiments (if possible).	Fracture parameters of cohesive elements are approximated from references.
Particles have various shapes and sizes.	Particles are modeled as regular pentagon of side length ~36 μm.
Millions of particles strike the coating to cause erosion.	Simulations are carried out up to six particles due to computational limitations.

Table 4
Assigned separation energy and reference displacements within different phases and interfaces.

Phases	Γ_o (J/m^2)	δ_n^* (nm)
YSZ	10	0.845
CoNiCrAlY	100	2.89
Oxide (Al$_2$O$_3$)	10	0.632
Interface of YSZ-CoNiCrAlY	30	1.519
Interface of YSZ-Oxide	10	0.716
Interface of CoNiCrAlY-Oxide	30	1.27

relates to the maximum separation stress as $\Gamma_o = e \delta_n^* \sigma_{max}$. Here e is the exponential function and σ_{max} denotes the peak stress during the separation of two surfaces (i.e., to crack). Note that for elastic–plastic material, the total fracture energy is the sum of this and associated plastic dissipation. For simplicity, the effect of mode-mixity on the separation energy is not considered but it can be easily included with an additional parameter [21]. Explicit relations between traction and separation relations for normal and shear are derived through partial derivatives of Φ with respect to δ_n^* and δ_t^*, respectively as,

$$T_n = \sigma_{max} \left(\frac{\delta_n}{\delta_n^*} \right) e^{1 - (\delta_n/\delta_n^*) - (\delta_n/\delta_n^*)^2}, \tag{2}$$

$$T_t = 2\sigma_{max} \frac{\delta_n}{\delta_t^*} \frac{\delta_t}{\delta_t^*} \left(1 + \frac{\delta_n}{\delta_n^*} \right) e^{1 - (\delta_n/\delta_n^*) - (\delta_t/\delta_t^*)^2}.$$

In the present study, the thickness of cohesive element is set as 0.01 μm, which is about 4% of the size of smallest element in the model.

Since limited measured data is available for the surface separation energy of thermal sprayed materials, they are approximated as shown in Table 4 based on some reported values [23–25]. Here the separation energy of metal phase (CoNiCrAlY) is set 10 times the ceramic phases (YSZ and oxide) while that along interfaces of ceramic and metal phases are set 3 times of those along the interface of two ceramic phases. Other values were also tested but we found the erosion behavior to be minimally affected by small changes in the separation energies. As expected, most of crackings occur within the ceramic phases and along their interfaces. In fact, the only type of cracking observed within the CoNiCrAlY region is when a large crack forms in YSZ phase advances through the metal phase. Nonetheless, to retain the consistency in distributions of cohesive elements among different models, they are kept throughout each model. The value of δ_n^* is set so that the initial modulus of cohesive element (computed via (2) for given Γ_o) coincides with the Young's modulus of the material (average if between two different phases). One of the potential errors in using cohesive element approach is the introduction of artificial compliance when spring type elements are utilized [22]. Since the cohesive behavior is modeled in the 4-noded solid elements here (with the same modulus as adjacent elements), such an error is alleviated. As impact occurs and large stresses develop, element boundaries are separated to simulate a crack. In the calculations, the cohesive elements are deleted from the model (to form a permanent crack) once the normalized separation energy reaches $\Phi/\Gamma_o = 0.9$. The deletions of elements reduce the numerical instability associated with element separations.

4. Computational results and discussions

4.1. Single particle impact

In order to isolate effects other than those of mixed metal phase and multiple particle impacts, initial simulations are carried our with the YSZ only model (Specimen A) under single particle impact. Using the mesh generated for this specimen, the alumina particle is impacted onto the top surface. In the simulation, the initial particle
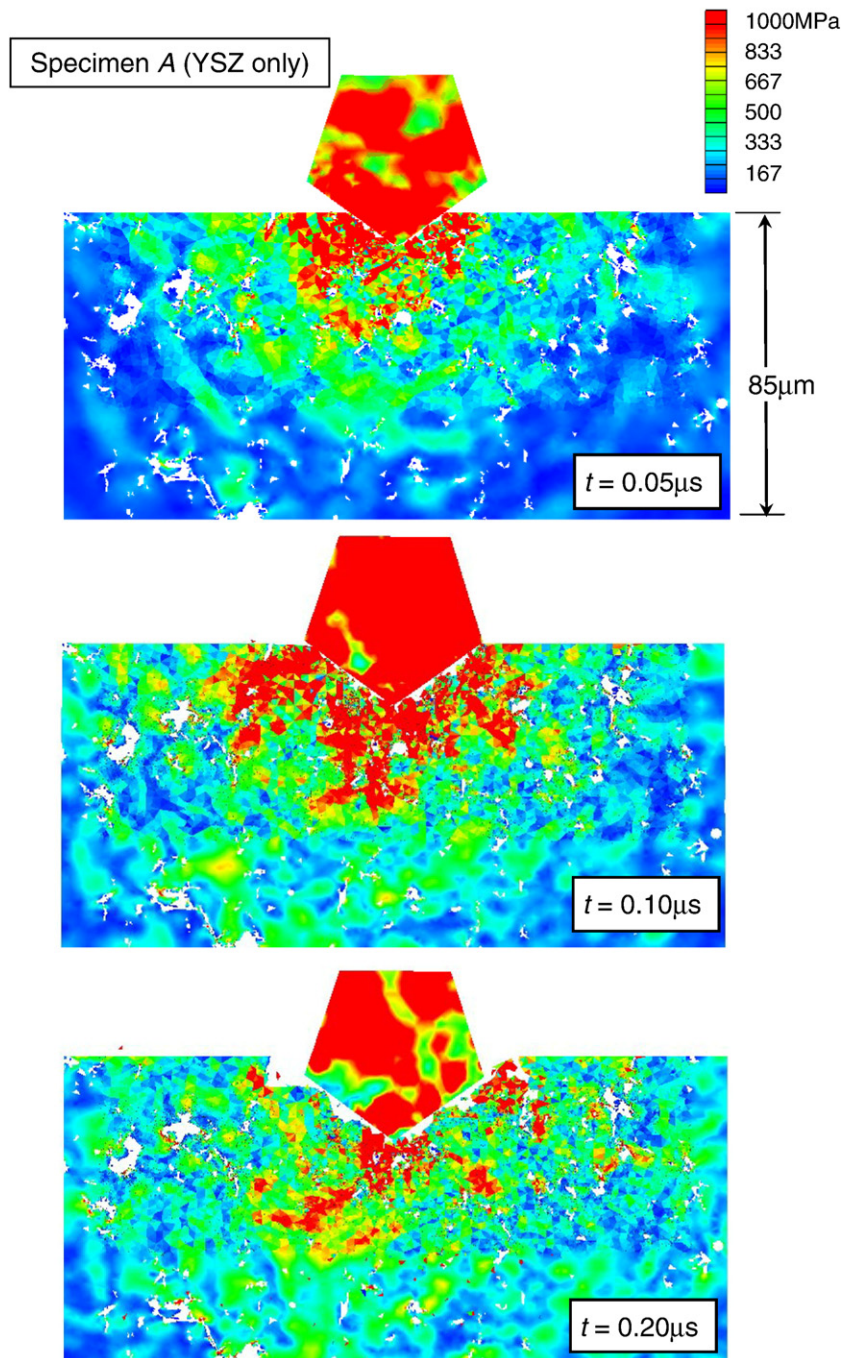
Fig. 7. Shades of effective stress showing progression of erosion by single particle impact with velocity, $v = 200$ m/s.

velocity is varied to study its effects. Evolution of computed effective stress after the impact with the initial particle velocity, $v = 200$ m/s is shown in Fig. 7. The porous morphology of coating causes the stress to spread discontinuously from the impact point. The figure also illustrates the material removal underneath the particle as it chips away YSZ coating. The particle penetrates into the coatings to about 25 μm deep and begins to bounce back/upward at the elapsed time of $t = 0.20$ μs. At this point, the magnitudes of stresses are already less than those at $t = 0.10$ μs.

4.2. Effects of pores and impact location

Since the microstructure is modeled as inhomogeneous as in the real specimens, material removal or erosion is highly dependent on

the morphology of coatings directly underneath the particle impact. To investigate such an effect, the specimen is impacted at five different locations. They are denoted as Locations 1–5 with each of them separated by 20 μm. The amount of material removal is represented by computing area/domain removed by a single particle impact as shown in Fig. 8. The results show a large variability in the eroded areas (white bars) especially with the initial particle velocity $v = 100$ m/s. The singly large erosion at Location 3 is attributed to a relatively large pore located under the impact (see center surface of Specimen A in Fig. 2). In order to gauge the influence of pores, a separate model was also created without any pores. In this model, all pores and cracks are filled with additional elements (with YSZ property) while the original elements representing YSZ phase were unchanged. As shown in Fig. 8 (a), although some variability still exists, it is substantially reduced in
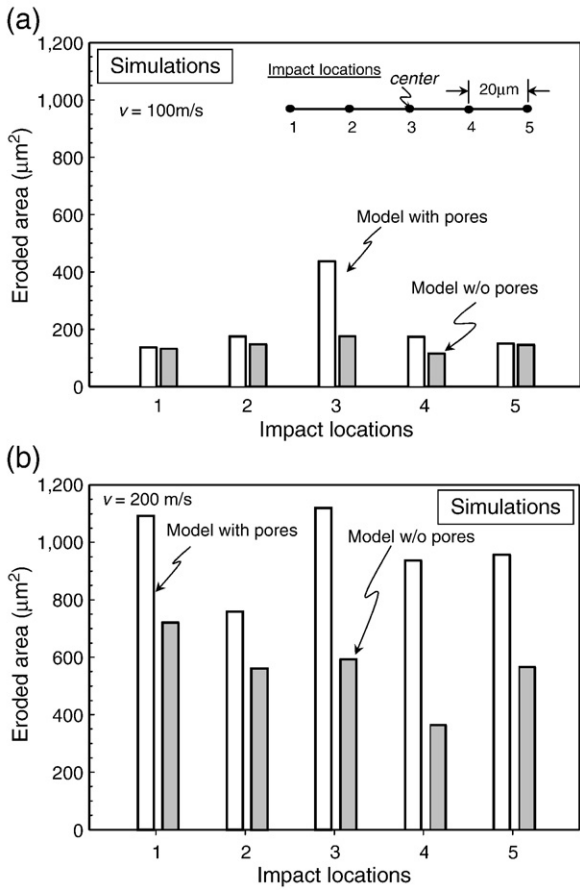
Fig. 8. Areas eroded in single impact simulations at various locations in Specimen *A* (YSZ-only). The results are shown for models with and without pores. Initial particle velocity is (a) $v = 100$ m/s, and (b) $v = 200$ m/s.

the model without pores (shaded bars), and also the magnitudes are less than those with pores.

With the higher initial velocity of particle ($v = 200$ m/s) shown in Fig. 8(b), the erosion rate appears to increase fourfold. This suggests the erosion rate to be nearly proportional to the square of velocity or the kinetic energy of particle. The relative variability appears to decrease at higher particle velocity. Though not conclusive, it may be due to the fact that larger areas are removed under the higher velocity impact. Since average effects of pores are likely to be more consistent when larger areas are removed than when smaller small areas are removed (e.g., lesser scattering of porosity), more consistent erosion can be observed. The erosion in model without pores is again substantially less than those in the model with pores. The results suggest the critical role of pores/cracks in the erosion mechanism.

Although not shown here we have investigated the effects of impact at an angle other than normal (90°). In the model without pores, the erosion is maximal at 90° impact angle, which is a typical response in homogeneous brittle materials. However in the model with pores, the highest erosion rate does not always occur at 90°. In fact it varies between 60° and 90° depending upon the pore morphology underneath the impact. Unlike homogeneous materials, it appears that the porous microstructures play an important role in defining the erosion behavior. These off-angle effects can be studied more comprehensively in the future studies.

4.3. Effects of ductile metal phase

After various simulations are performed on the YSZ-only specimen (*A*), similar calculations are carried out with the other two specimen

models containing metal phase (*B* and *C*). The computations are performed for four different impact velocity at $v = 50, 100, 150$ and 200 m/s. Since the location of impact influences the amount of erosion, simulations are carried out at various impact locations for a given impact velocity in each specimen and averaged. The averaged values of eroded area are shown as functions of initial velocity of particle in Fig. 9 (a). Here the error bars represent variations among different locations. At the low impact velocity (50 m/s), the differences among three models are negligible as only near surface YSZ phase is removed by the impacting particle. At higher velocities, the effects of ductile phase are more pronounced showing smaller erosion in Specimens *B* and *C*. The simulation also captures a greater erosion resistance in the model with greater metal phase (Specimen *C*) though the relative resistance change is not as much as the measured results shown in Fig. 5. The discrepancy may be attributed to the following reasons. First, the simulations represent only single particle impact condition whereas the test data is obtained after multiple particle impacts. Second, the computational models are two-dimensional, and it may constrict the effects of ductile phase. Essentially, in 2D model, the *area* removal is computed while in real specimens, the *volume* removal is measured. Nevertheless, the present simulations offer qualitative insights into the increased erosion resistance with the ductile phase addition (more discussions in Section 4.4).

The erosions under different impacting particle velocities are also compared with the particle's kinetic energy (per thickness) as shown in Fig. 9(b). Here the kinetic energy is shown in terms of per unit thickness since the particle and coatings are modeled in 2D. Interestingly, the curves are nearly linear which suggest a proportional relationship between the erosion and the kinetic energy of particle.
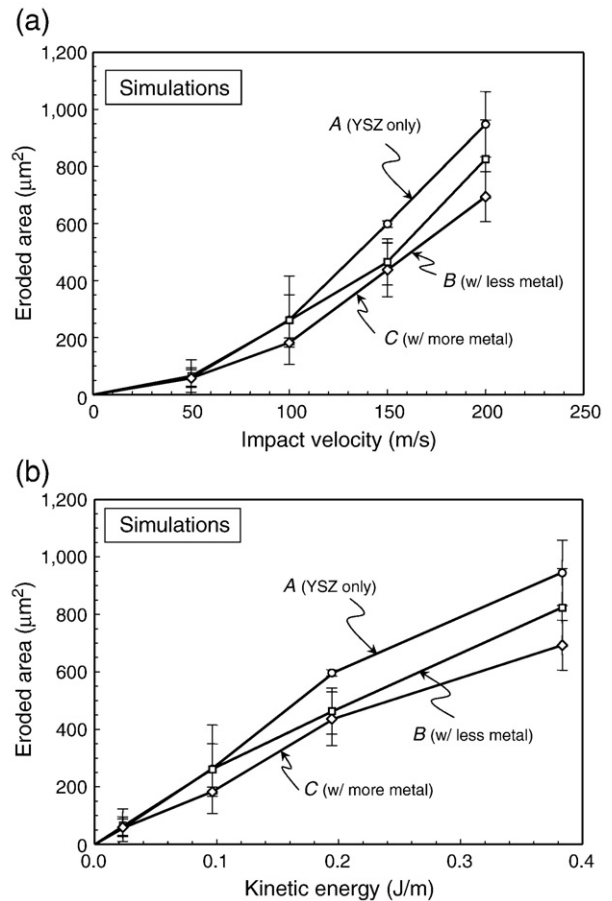

Fig. 9. Areas eroded by single particle impact for different specimen models. Shown as a function of (a) impact velocity and (b) kinetic energy (per thickness) of particle.
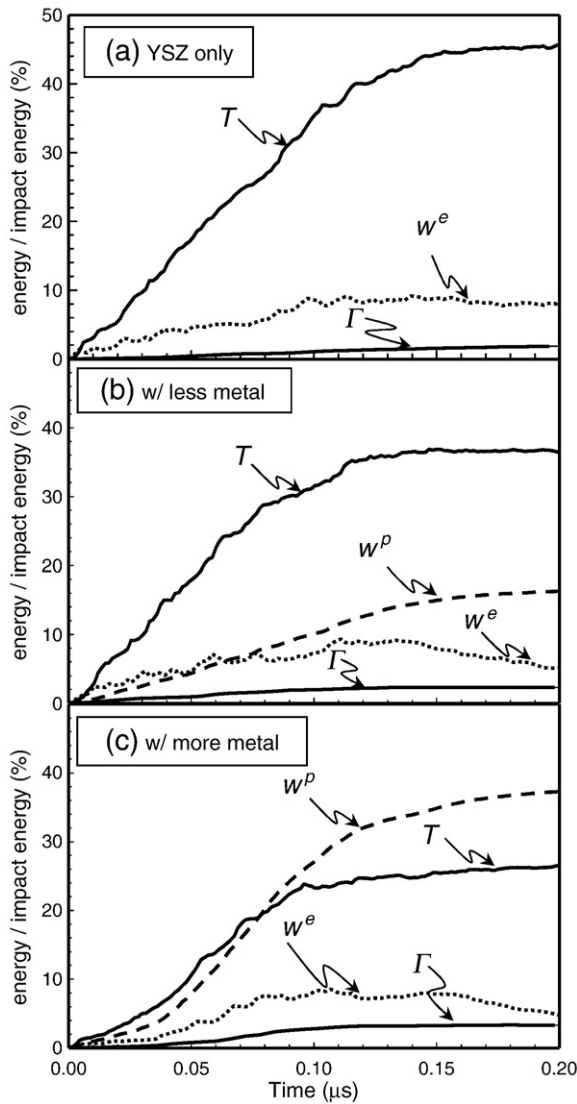
Fig. 10. Energy components normalized by initial kinetic energy of impacting particle ($v = 200$ m/s) shown as function of elapsed time for three different specimens.

In Specimen *A* without the metal phase, there is no plastic dissipation. Here the kinetic energy T, elastic strain energy W^e, and total fracture/separation energy Γ of target coating are shown as functions of time after initial impact. In this purely elastic coating, the energy transfer from the particle to the coating is nearly proportional to the elapsed time at least until ~0.10 μs. Nearly one half of the impact energy of particle is transferred to the kinetic energy (T) of coating by this time. Surprisingly, the total separation energy remains lows (<2%) even though many cracking and fragmentations have occurred by this time (see Fig. 7). This is caused by a low critical separation energy is low ($\Gamma_o = 10$ J/m²). Thus even with large delaminated surfaces, the total separation energy remains relatively small. When the penetration by the particle is halted at t ~ 0.20 μs, slightly more than half of the impact energy remains as recoverable energy (T and W^e). However, they include those of delaminated or chipped away segments. In fact about 80% of kinetic energy is contributed from already fragmented particles. Note all the energy parameters do not sum up to 100% since appreciable amounts of kinetic and elastic energies remain in the impacting particle.

The energy evolutions in the specimens with metal phases are clearly different from those of Specimen *A* as shown in Fig. 10. First, it is clear that substantial amount of impact energy is absorbed as plastic dissipation. In the model with greater metal phase (Specimen *C*), a third of the energy is consumed as plastic deformation. Second, the behavior of elastic strain energy is little affected by the metal phase while that of the kinetic energy shows significant decline. In addition, at the end of penetration, the impacting particle has lesser energy (i.e., a greater energy is transferred from the particle to coating). Third,
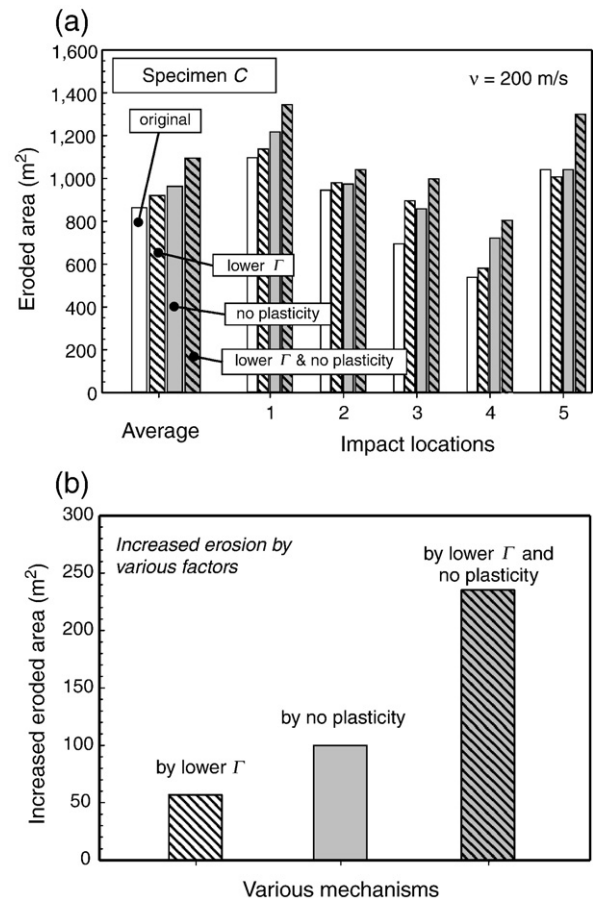
Though not presented here, we have also carried out other simulations with YSZ model without pores (solid model) and found the eroded areas to be almost exactly proportional to the kinetic energy of striking particle. These results support the linear correlations between the erosion and kinetic energy of particle [1].

4.4. Erosion mechanisms in ductile phase

As observed in the experiments as well as in the computational results, the addition of metal phase improves erosion resistances of TS coatings. Two likely sources of erosion mechanisms in the ductile (CoNiCrAlY) phase are the high fracture toughness and plastic dissipation. The latter mechanism absorbs the kinetic energy of impacting particle and reduces the energy available for material removal. In fact the evolutions of various energy components play important role in defining erosion mechanics. In order to investigate how the energy transfer occurs from the striking particle's kinetic energy, the behavior of various energy parameters were computed as shown in Fig. 10 for the three specimens. In each plot, the results represent averaged energies from three different impact simulations (under the particle velocity of $v = 200$ m/s). Each component is normalized by the kinetic energy of striking particle (0.384 J/m).

Fig. 11. Effects of fracture energy and plasticity in metal phase: (a) Total eroded area of various models with different impact locations and their average. (b) Net increases in erosion due to various factors.

although the total fracture energy is still relatively low, it is much higher here (3.2% in C at $t = 0.2$ μs)) than Specimen A (1.9%). Even though majority of cracking occurs within YSZ (or oxide) phase, some delamination along metal-YSZ/oxide interfaces and within metal phase contributed to the larger energy dissipations. Taking advantage of computational ability to investigate the underlying erosion mechanisms, the coating model (Specimen C) is modified to quantify the effects of two key factors. They are the fracture resistance and the plastic flow. First, the separation energy assigned to CoNiCrAlY as well as all the interfaces (see Table 4) is lowered to be equal to that of YSZ (i.e., $\Gamma_o = 10$ J/m^2). The simulations are then carried out by impacting at five different locations, and computed eroded areas are shown (as "lower Γ" model) in Fig. 11(a). In the second model, the separation values are unchanged but the plasticity of metal (CoNiCrAlY) is suppressed (i.e., linear elastic model) while the Young's modulus is unchanged. The results are denoted as "no plasticity". In the third model, labeled as "lower Γ and no plasticity", the separation energy is reduced and no plasticity is assumed. Note that "original" denotes the model with the original separation energy (Γ) and plasticity conditions. For each model, the average from five impact locations is shown since large variations exist depending upon the location of impact. These results clearly show the erosion to increase as the condition is changed from "lower Γ", "no plasticity" to "lower Γ and no plasticity".

To investigate these phenomena further, their net effects are obtained by subtracting the eroded area of original model (with higher Γ and plasticity) from each model using the average values as shown in Fig. 11(b). Essentially, these results represent the erosion increases due to lowering Γ and no plasticity. Alternatively, they can be regarded as the influencing factors to enhance erosion *resistance* (with the metal phase inclusion). For individual conditions, the plasticity effect (10% of total) is higher than that of delamination energy (6%). However, the combined conditions show a synergistic effect with a greater erosion resistance (23%) than the sum of two individual conditions. The normalized energy components at $t = 0.20$ μs are also listed in Table 5. Here lowering delamination resistance not only reduces the total delamination energy from 3.2% to 2.5% but also decreases the plastic deformation from 39% to 32%. The resulting effect is the larger eroded area. Without the plasticity, the total delamination energy is substantially increased from 3.2% to 4.9% (due to cracking along metal-YSZ/oxide interfaces and within metal phase) but the erosion resistance is reduced without plastic dissipation. Although a conclusive statement can not be made from the single particle analysis, these results should offer useful information to understand the increased erosion resistance with inclusion of metal phase.

4.5. Multiple particle impact

In the previous section, the results of single particle are used to extrapolate the erosion behavior. Although some underlying behaviors are clarified, the single particle simulation lacks physical factors critical in real erosion. First, except during the initial phase, particles strike onto non-flat surfaces left by previous impacts. Second, a single particle model does not consider the residual damage by earlier impacts (e.g., embedded cracking and residual strains in metal phase).

Table 5
Energy components (at $t = 0.20$ μs) normalized by the same initial kinetic energy of impacting particle for various modified models.

Models	T (%)	W^e (%)	W^p (%)	Γ (%)
Original (Specimen C)	25.8	5.5	39.3	3.2
Lower Γ	35.5	5.8	32.2	2.5
No plasticity	46.0	10.3	0.0	4.9
Lower Γ and no plasticity	50.1	8.6	0.0	3.0

Specimen A (YSZ only)

(a)

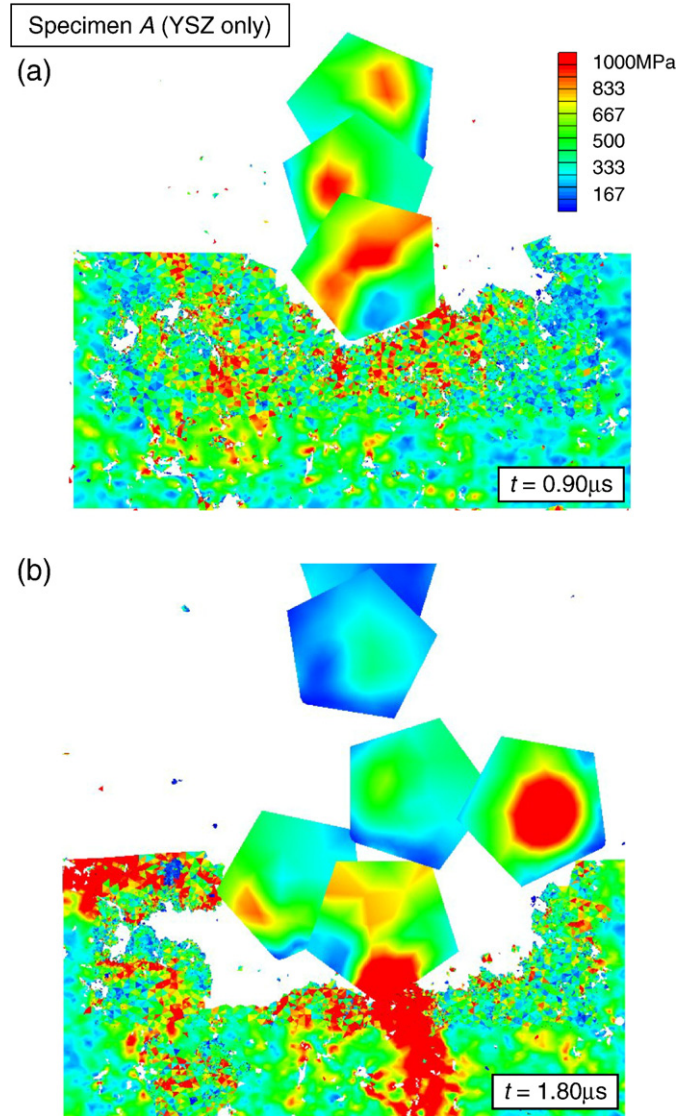| | 1000MPa |
	833
	667
	500
	333
	167

$t = 0.90$ μs

(b)

$t = 1.80$ μs

Fig. 12. Shades of effective stress showing progression of erosion by multiple particle impacts ($v = 200$ m/s.), after (a) three impacts, (b) six impacts. Small fragmented particles scattering away can be observed.

To study these effects, simulations are carried out to impact the coating models with six particles. Although simulations with greater particle impacts would provide more valuable results, such a study would require a larger model (due to greater eroded region) and much greater computational resources. A large number of particle strikes also tend to generate convergence and numerical difficulties as chances of instability due to large element distortion grow. Thus the present analysis is limited to six particle impacts.

The analysis is carried out as follows. The first particle impact is set to occur at the center of specimen. The locations of subsequent impacts are chosen randomly within the span of ± 25 μm from the center although the interval of impact is fixed at $t = 0.3$ μs. The interval was set small enough to minimize the computational effort but long enough to avoid interactions with the preceding particle. Based on the single particle analysis, the duration of impact process lasts for about $t = 0.2$ μs. Illustrations of erosion on Specimen A after 3 and 6 particle impacts are shown in Fig. 12. In each plot, apart from the particle at the lowest position, the particles have bounced back and are moving upward.

Eroded profiles after six particle impacts are shown in Fig. 13. With the multiple impacts, the depths and widths of erosion are more than
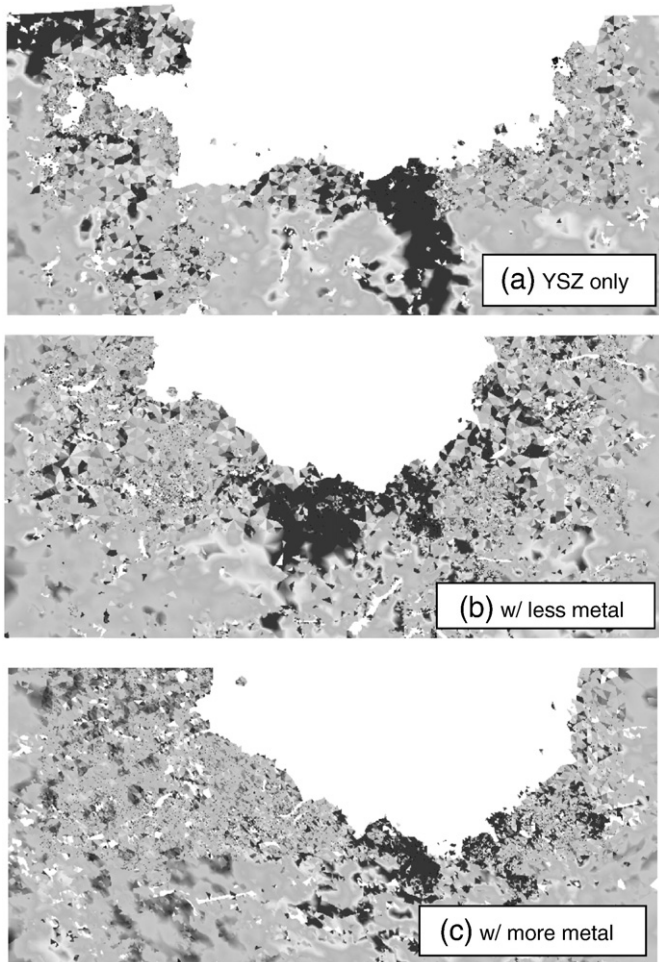
Fig. 13. Eroded profiles after six particle impacts for the three coating models.

mechanisms responsible for erosion process, computational models were constructed. Here TS coatings' heterogeneous microstructures were directly modeled from the SEM micrographs. Compared to fully dense or solid models, existences of pores and cracks greatly accelerate the erosion or the material removal. Essentially, sections of coatings can be broken off upon particle strikes and coatings are more prone to fracture.

In the present models, due to the inhomogeneity of microstructures, the results are highly sensitive to the morphology beneath impact. Thus, to characterize the erosion behavior, several cases were analyzed and their averages were reported. From these averaged values, the present computational analyses were able to confirm a higher erosion resistance condition in a model containing a ductile phase.

The computational analysis also enabled us to identify two mechanisms responsible for increased erosion resistance of coatings with ductile phase mixture. One is larger fracture resistances along the metal-YSZ/oxide boundaries and within the metal phase. Not only they make cracking more difficult by acting as barriers to crack growths but if they crack, more energy is dissipated (to absorb striking particle's energy). The other mechanism is the plastic deformation. Here, the incoming energy of particle is absorbed by the plastic dissipation of metal phase. More interesting result is the synergistic effect of the two. The larger fracture resistance of metal phase enhances the plastic deformation which leads to even greater erosion resistance than the sum of the two individual mechanisms. In summary, the ductile phase in coatings absorbs the impact energy through its plastic deformation and also hampers cracking with its large fracture toughness. These results may be useful in identifying an optimal mixture of ductile phase. For an example, to enhance the erosion resistance, it may not be always beneficial to use a metal phase with a low yield stress (to increase plastic flow) but the one with higher fracture toughness may be better. In addition, a large amount of metal phase may increase the erosion resistance but it would also lower the coating performances at high temperature environment. These factors must be taken into account in selecting the optimal mixture.

Since certain features were idealized and approximated, the present computational results must be treated carefully. Additional analyses were carried out to ensure that these idealizations did not lead to erroneous results. Here the results were checked with some known solutions and the consistency in results was monitored. Due to the complexity of model, the erosion process was modeled only near the free-surface. However as the erosion progresses, longer tangential and lateral cracks may develop beyond the region which can accelerate the material removal and significantly reduce the coating integrity. Such a phenomenon may be studied in the future.
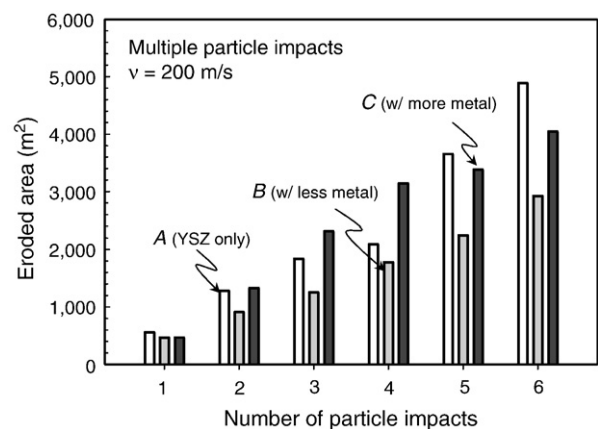
double of the single impact results shown in Fig. 7. However, the eroded profiles are still sensitive to the morphologies underneath the locations of impacts. The eroded areas are computed after each impact as shown in Fig. 14. All specimens exhibit continuous increases in erosion. Here the first impact causes slightly larger erosion in Specimen A than those of the other two specimens with metal phase (B and C). However, greater erosion occurs in Specimen C during the next three impacts (2–4) and shows a greater eroded area than that of YSZ-only model (Specimen A). Also, a jump in erosion occurs in Specimen A with 5th impact, which removes a large chunk of coatings. After six particle impacts, the accumulated erosion is largest in Specimen A while Specimen B with less metal phase has the lowest erosion. Due to the inhomogeneous nature, these results are dependent on the impact locations and microstructure near the impact. Since the results are highly statistical, a rigorous study with many simulations under various conditions would be needed to reveal more accurate behaviors. Nonetheless, the multi-particle analysis shows consistent erosion increases with particle impacts, which support the validity of present computational model and procedure (even for non-flat surface impacts and models with residual damage).

5. Conclusions

The present study consisting of experimental and computational analyses offers insights to erosion mechanisms of predominantly brittle thermally sprayed coatings. First, the experimental results showed significant improvements in erosion resistances when ductile metal phase was added to TS YSZ coatings. Next, to probe the physical

Fig. 14. Progressions of eroded areas as six particles are sequentially impacted onto coatings. The results are shown for three separate specimen models.

It is also known that the hardness of coating correlates with the erosion resistance. Similar models can be used to estimate the hardness of TS coatings under quasi-static loading. However, if cracking behavior is included, the computational simulations may face a difficulty in achieving numerical convergence. Often the inertia effects in the dynamic analysis help to obtain more stable solutions.

In summary, the current study represents an initial step toward elucidating the complex erosion mechanisms of porous heterogeneous material systems/coatings. A similar approach should be useful in qualitative evaluation of foreign object damage of coatings that occur in many engineering applications.

Acknowledgements

References

[1] I. Finnie, Wear 186–187 (1995) 1.
[2] S. Usmani, S. Sampath, JOM J. Minerals Matals Materials Soc. 48 (11) (1996) 51.
[3] A.G. Evans, M.E. Gulden, T.R. Wilshaw, Acta Metall. 24 (1976) 343.
[4] J.R.T. Branco, R. Gansert, S. Sampath, C.C. Berndt, H. Herman, J. Mater. Res. 7 (1) (2004) 147.
[5] I. Finnie, Y.H. Kabil, Wear 8 (1) (1965) 60.
[6] Y. Wang, Z. Xu, Surf. Coat. Technol. 200 (12–13) (2004) 3896.
[7] H.I. Faraoun, T. Grosdidier, J.L. Seichepine, D. Goran, H. Aourag, C. Coddet, J. Zwick, N. Hopkins, Surf. Coat. Technol. 201 (6) (2006) 2303.
[8] D. Sporer, S. Wilson, I. Giovannetti, A. Refke, M. Giannozzi, Thirty Sixth Turbomachinery Symp. Proc. 79, 2007.
[9] N.S. Stoloff, C.T. Liu, S.C. Deevi, Internet 8 (9–11) (2000) 1313.
[10] B.A. Cook, A.M. Russell, J.L. Harringa, A.J. Slager, M.T. Rohe, J. Alloy. Comp. 366 (1–2) (2004) 145.
[11] Z. Yin, S. Tao, X. Zhou, C. Ding, Appl. Surf. Sci. 254 (6) (2008) 1636.
[12] Y. Dong, D. Yan, J. He, X. Li, W. Feng, H. Liu, Surf. Coat. Technol. 179 (2–3) (2003) 223.
[13] S.O. Chwa, D. Klein, F.L. Toma, G. Bertrand, H. Liao, C. Coddet, A. Ohmori, Surf. Coat. Technol. 194 (2–3) (2005) 215.
[14] A.P. Harsha, A.A. Thakre, Wear 262 (7–8) (2007) 807.
[15] T. Sinmazcelik, I. Taskiran, Mater. Des. 28 (9) (2007) 2471.
[16] K. Tsuda, M. Kubouchi, T. Sakai, A.H. Saputra, N. Mitomo, Wear 260 (9–10) (2006) 1045.
[17] Q. Chen, D.Y. Li, Wear 255 (1–6) (2003) 78.
[18] ASTM G76-07, ASTM International, 2007.
[19] Y. Gu, T. Nakamura, Mech. Mater. 39 (4) (2007) 340.
[20] V. Tvergaard, J.W. Hutchinson, Int. J. Solid. Struct. 33 (1996) 3297.
[21] X.P. Xu, A. Needleman, J. Mech. Phys. Sol. 42 (9) (1994) 1397.
[22] Z. Wang, T. Nakamura, Mech. Mater. 36 (7) (2004) 601–622.
[23] E.P. Busso, Y.V. Tkach, R.P. Travis, Mater. Res. Soc. Symp. Proc. 594 (2000) 31.
[24] A.M. Khoddami, A. Sabour, S.M.M. Hadavi, Surf. Coat. Technol. 5 (2007) 6019.
[25] W.G. Mao, C.Y. Dai, Y.C. Zhou, Q.X. Liu, Mech. Mater. 38 (2006) 1118.